



Study of the electrostatic jet initiation in near-field electrospinning

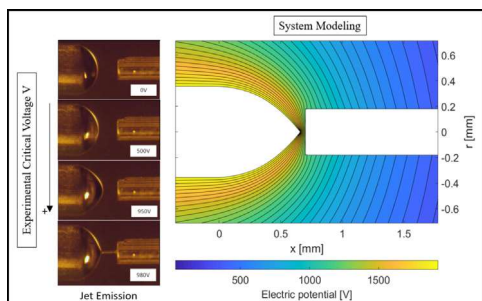
Albert Cisquella-Serra ^{a,b,1}, Marco Magnani ^{a,1}, Álvaro Gual-Mosegui ^a, Sunshine Holmberg ^b, Marc Madou ^{a,b}, Manuel Gamero-Castaño ^{a,*}



^a Mechanical and Aerospace Engineering, University of California, Irvine, CA 92617, USA

^b Materials and Manufacturing Technology, University of California, Irvine, CA 92617, USA

GRAPHICAL ABSTRACT



ARTICLE INFO

Article history:

Received 14 December 2018

Revised 10 February 2019

Accepted 11 February 2019

Available online 13 February 2019

Keywords:

Electrospray

Electrospinning

Near-field electrospinning

ABSTRACT

Hypothesis: The electrostatic initiation of a jet from the meniscus of a polymeric solution is a key step in near-field electrospinning (NFES), however this process is not sufficiently understood to determine a criterion for the critical emitter voltage triggering the jet, nor to optimize the electrodes. It is expected that the jet initiation in NFES is similar to that in cone-jet electrosprays, and can be described with a first principles model.

Experiments: The electrostatic jet initiation of an SU-8 polymeric solution is studied with two different electrode geometries to quantify the initiation parameters and illustrate the optimization of the electric field. A first-principles model is developed to predict and analyze the initiation.

Findings: Two jet emission mechanisms are identified: one in which the jet is ejected from a free-standing conical meniscus; and one resulting from the contact of the meniscus with the collector, as it evolves from a spherical to a conical shape. Both are triggered by a critical emitter potential. The former produces the thinnest jets with a diameter that depends on the properties of the fluid, while the latter is an alternative to existing mechanical initiation methods. The model reproduces well the experimental phenomena including the critical voltage.

© 2019 Elsevier Inc. All rights reserved.

1. Introduction

Electrospinning is a technique for producing long microfibers from a liquid solution [1]. It applies the jetting ability of an electrospray to liquid solutions with high concentrations of polymers. The resulting viscoelastic nature of the fluid is essential to inhibit the natural instability of the jet and its tendency to disintegrate. An

* Corresponding author at: S4232 Engineering Gateway, Mechanical & Aerospace Engineering, University of California, Irvine, CA 92697-3975, USA.

E-mail address: mgameroc@uci.edu (M. Gamero-Castaño).

¹ These authors contributed equally to this work.

electrospray and its jet naturally develop from a liquid drop under the influence of a strong electric field, which induces the external stress required to balance the high capillary tension resulting from the jet's curvature [2,3]. An important feature of electrosprays is that the diameter of the base of the jet only depends on the physical properties of the fluid (surface tension, electrical conductivity, and density) and its flow rate. In addition the electric field acting on the charge migrated to the surface accelerates the jet, thinning it down for as long as it remains stable. Thus, by operating with the appropriate combination of fluid properties and electric field strength, jets with diameters ranging from several micrometers to tens of nanometers can be generated regardless of the diameter of the nozzle feeding the fluid, and the associated fibers can be drawn into intricate microarchitectures. The speed and flexibility of electrospinning have led to applications in numerous fields as diverse as tissue engineering [4,5], drug delivery [6], filtration [7,8], gas sensors [9,10], optical and photoelectric sensors [11], and catalysis [12].

Over the last decade a significant effort has been made to adapt electrospinning into a controlled nano-writing process with the capability of rapidly patterning submicron features. This work has led to a variant of electrospinning known as near-field electrospinning (NFES) [13,14]. NFES reduces the distance between needle and collector to a few millimeters, avoiding bending instabilities and the associated random motion of the jet typical in traditional electrospinning [15]. Thus, whereas traditional electrospinning results in mats of micro or nanofibers, NFES is characterized by single fiber deposition with high spatial resolution. NFES has shown great potential for producing controlled sub-micron fibers of polymers, carbon and ceramic materials [6,16]. NFES can also be integrated with other microfabrication processes such as lithography to generate more complex patterns [17,18].

Most of the research on NFES has focused on the analysis of the properties of the generated fibers and fiber patterns [19,20], while the physics behind NFES has received less attention. In our experience successful NFES operation is largely based on the user's familiarity with the technique and trial and error practices, probably due to the lack of a fundamental understanding of the processes involved. For example, a key step in NFES is the initiation of the jet. Lin and collaborators, in their landmark article originating the field, initiate the jet by simply increasing the voltage difference between a metallic needle holding a pendant drop, and a facing grounded plane [13]. This is the standard way of initiating electrosprays, for which the jet's onset or critical voltage V_o scales with the surface tension γ of the fluid and the radius R of the liquid drop as $V_o \approx (2\gamma R/\varepsilon_0)^{1/2}$, where ε_0 the permittivity of vacuum. However this standard initiation method in NFES typically results in undesired outcomes such as the discharge and deposition of most of the drop or multiple fibers, and a lack of control on the deposition of the fiber due to bending instabilities of the jet. To overcome this problem mechanical initiation methods have been developed based on piercing the drop with a sharp glass or metal needle before or coinciding with the application of an electric field, and dragging the attached fluid bridge to the deposition plate [17,21,22]. Mechanical initiation is difficult to reproduce and leads to large variations in the diameter of the fibers [23]. Furthermore some studies point to the need of critical electric fields one order of magnitude higher in NFES than in traditional electrospinning, e.g. 10^6 V/m versus 10^5 V/m [22], which is paradoxical because the local electric field at the apex of the meniscus required to initiate the jet should only be a function of the properties of the fluid, and not of the dimensions of the emitter and collector. It is apparent that a better understanding is needed to rationalize why the simpler standard initiation usually fails in NFES; devise conditions compatible with standard initiation if possible; obtain reliable laws

for the diameter of the jet and fibers; and generally, optimize NFES on the basis of first principles.

This article analyzes the jet initiation phenomenon in NFES. We elaborate a physical model for computing the shape of the liquid meniscus in the presence of an electric field, and for predicting the critical voltage for given fluid properties and geometry of the emitter and collector electrodes. The results of the model compare well with experimental data obtained with a polymeric solution which, upon thermal treatment of the collected fibers, yields glassy carbon wires [18]. Although the model allows for a general geometry, the study focuses on two distinct configurations: the basic capillary emitter facing a planar collector; and this geometry with an additional dielectric rod placed between the emitter and the collector. Experiments show that NFES is favored by the second configuration, an observation that is rationalized with the model.

2. Materials preparation and experimental methods

The jet initiation experiments are carried out with a polymeric solution made by mixing SU-8 2002 from MicroChem. Inc., with 0.75 wt% of high molecular weight (MW = 4,000,000) polyethylene oxide (PEO) from Dow Inc. (WSR-301), and 1 wt% tetrabutylammonium tetrafluoroborate (TBF). The SU-8/PEO/TBF blend is diluted with 30 vol% of N,N-Dimethylformamide. This polymer solution is electrospinnable and pyrolyzable [17]. The properties of the resultant fibers after pyrolysis yield glassy carbon wires, which have been recently analyzed [18]. While the SU-8 component, after crosslinking with UV light and performing pyrolysis, produces the glassy carbon phase, the PEO component provides the viscoelastic properties needed for electrospinning. The ratio SU-8/PEO is critical, since an excess of PEO will not allow carbonization of the fiber during pyrolysis due to oxygen content.

Fig. 1 is a sketch of the experimental set up used in the characterization of jet initiation. The polymeric solution is stored in a syringe protected from ultraviolet light to avoid crosslinking of the SU-8. A stainless steel capillary tube attached to the tip of the syringe channels the solution to the emission site, which takes place at the end of the capillary tube itself. The outer and inner diameters of the tube are 710 μm and 533 μm . The end of the line used as emitter is mounted inside a chamber that provides mechanical rigidity. A syringe pump drives the solution to the emission site, and is turned off once the fluid emerges and forms a visible meniscus. The size of the liquid meniscus, held at the tip by surface tension, can be modified by adjusting the height difference Δh between the pump and the emission site. The chamber has windows that allows the observation of the meniscus with a microscope housing a camera. Most experiments were recorded with a high-speed digital camera, and some with a standard digital camera. Ultraviolet filters placed on the windows avoid crosslinking of the SU-8. A brass disk with a diameter of 38 mm is used as a collector. It is mounted perpendicular to the emitter on an XYZ stage that, actuated with stepper motors, allows for incremental positioning with a resolution of 26.5 μm . The emitter is connected to a high voltage power supply, and the collector is grounded. The jet initiation experiments are done for two geometries: the simpler emitter/plate configuration; and placing a fused silica rod between the emitter and the disk, referred to as emitter/rod/plate configuration. The rod has a diameter of 340 μm , a typical length of 2.23 mm, and a dielectric constant of 3.77 (Polymicro Technologies, LLC). All the experiments are performed at atmospheric pressure and room temperature, between 22 °C and 24 °C.

Fig. 2(a) shows the evolution of the liquid meniscus in a typical jet initiation experiment, as the emitter potential is increased up to the value that triggers the formation of the jet. Although the experiment corresponds to the emitter/rod/plate configuration, the basic phenomena is common to the emitter/plate configuration. At zero

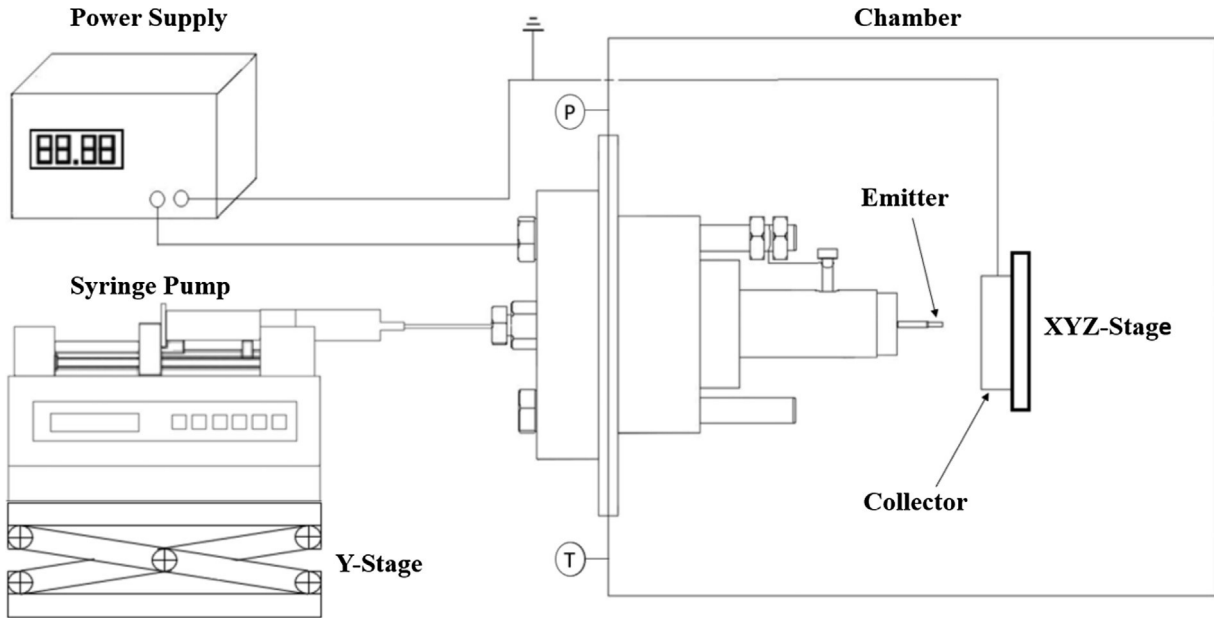


Fig. 1. Schematic of the experimental setup.

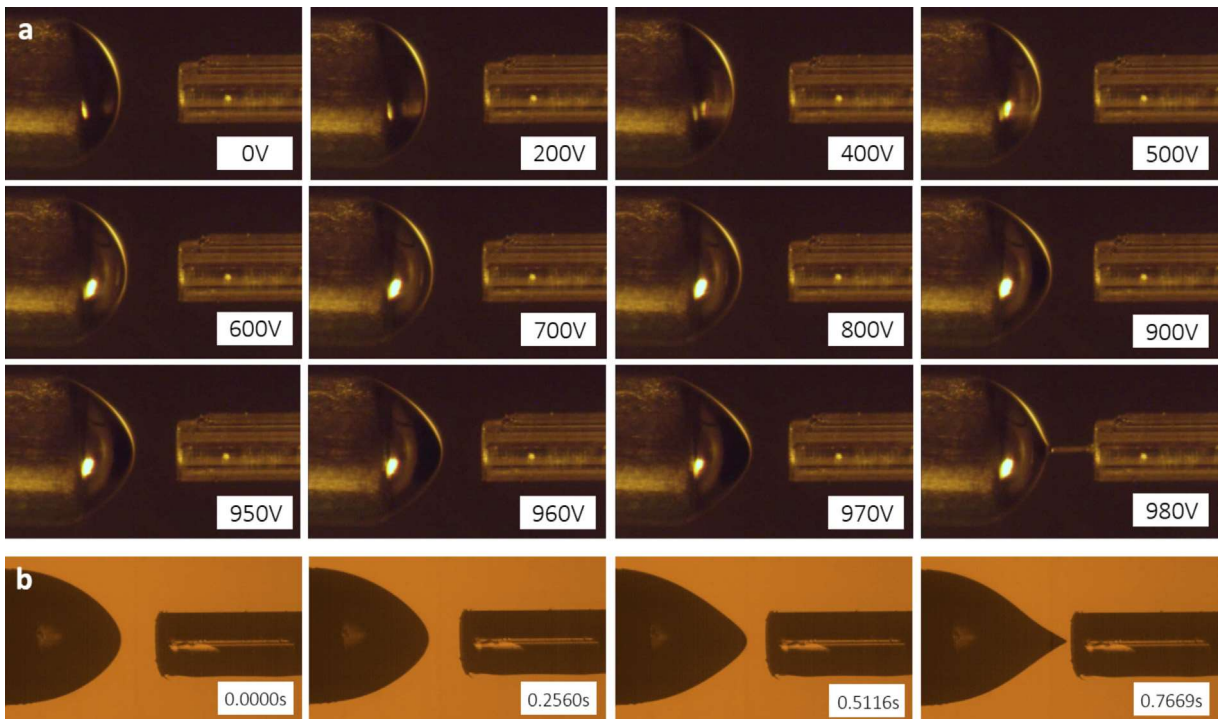


Fig. 2. Evolution of the liquid meniscus at increasing potential in the emitter/rod/plate configuration: (a) photographs at increasing voltage, up to the ejection of the jet; (b) high speed imaging of the fast evolution from spherical to conical meniscus preceding jet ejection.

potential the meniscus is spherical, with a shape that results from the balance of surface tension and the pressure head of the fluid. As the voltage increases the electrical stress pulls out the meniscus, while the surface retains the spherical shape. The displacement of the meniscus increases modestly up to a potential of 960 V, at which point a small increase in potential suffices to double the displacement: at 980 V the meniscus accelerates forward and touches the surface of the rod immediately before releasing the jet and pulling back. The last photograph in Fig. 2(a) shows the final, stationary state of the meniscus and jet at 980 V. Fig. 2(b) shows images of the meniscus during the sudden displacement leading to the ejection of

the jet, taken with the fast camera under near identical conditions: during a transient of a few hundred milliseconds the spherical tip of the meniscus turns into a conical shape before ejecting a jet. This minimum voltage that triggers an abrupt transition from a spherical to a conical meniscus from which the jet forms is observed in all experiments, and defines the critical voltage.

3. Jet initiation model

We next formulate a model, based on the work by Pantano et al., [24] to compute the position of the free surface and the elec-

tric field surrounding the meniscus, and ultimately to determine the critical voltage leading to the emission of the jet. Fig. 3 shows a sketch of the axisymmetric model domain. A hydrostatic liquid meniscus is attached to an emitter electrode of radius R , and has a free surface $X(r)$ determined by a balance between surface tension, pressure and electric stress. An electric field surrounds and acts on the meniscus, induced by a voltage difference ϕ_0 applied between the emitter and a ground electrode, and in some cases influenced by the presence of a dielectric rod. The domain is enclosed by a surface Σ_3 , while Σ_1 , Σ_2 and Σ_4 are the surfaces of the emitter, ground electrode and dielectric rod respectively. We next introduce the equations of the model in nondimensional form using R , γ/R and ϕ_0/R as the length, pressure and electric field scales; symbols topped with a tilde denote nondimensional variables. The position of the surface is given by the augmented Young-Laplace equation and boundary conditions:

$$\frac{\tilde{r}\tilde{X}'' + \tilde{X}' + \tilde{X}'^3}{\tilde{r}(1 + \tilde{X}'^2)^{3/2}} - \tilde{P} = \Pi_T \tilde{\mathbf{E}}_S(\tilde{r})^2 \quad (1)$$

$$\tilde{X}(1) = 0 \quad (2)$$

$$\tilde{X}'(0) = -\tan^{-1}(\theta_a) \quad (3)$$

P is the pressure in the liquid (constant throughout due to the hydrostatic assumption), and $\mathbf{E}_S(r) = \mathbf{E}(r, X(r))$ is the electric field on the surface. One end of the surface is attached to the rim of the emitter, while the angle θ_a with the axis is imposed at $r = 0$. The hydrostatic assumption requires a null electric field inside the fluid, and therefore an equipotential meniscus (the electric field is then normal to the surface). The electric field is derived from the electric potential, $\tilde{\mathbf{E}} = -\nabla\tilde{\phi}$, which fulfills the Laplace equation with boundary conditions:

$$\nabla^2\tilde{\phi} = 0 \quad (4)$$

$$\tilde{\phi}(\Sigma_1) = \tilde{\phi}_S(r) = 1 \quad (5)$$

$$\tilde{\phi}(\Sigma_2) = 0 \quad (6)$$

$$\frac{d\tilde{\phi}}{dn}(\Sigma_3) = 0 \quad (7)$$

i.e. constant potential at the surface of the liquid, emitter and plate, and symmetry conditions at the outer boundary.

The solution is a function of three dimensionless numbers: the dimensionless pressure \tilde{P} , the Taylor number $\Pi_T = \frac{\varepsilon_0\phi_0^2}{2R}$, and the angle θ_a ; and of geometric factors. For example, the spherical menisci in Fig. 2(a) are readily computed by solving this model with the applied voltage ϕ_0 , the pressure head P , and using $\theta_a = 90^\circ$. However a main goal of the model is to determine the critical voltage that initiates the jet or equivalently, and as illustrated by Fig. 2, makes the meniscus conical. Therefore three additional relations are needed to fix the values of \tilde{P} , Π_T and θ_a for the jet initiation condition. To this end we seek two closure relations by first approximating the surface near the axis with a second order polynomial

$$\tilde{X}(\tilde{r} \rightarrow 0) = \tilde{X}_0 - \frac{\tilde{r}}{\tan \theta_a} + \frac{\tilde{X}_0''}{2}\tilde{r}^2 + O(\tilde{r}^3) \quad (8)$$

which, inserted in the Young-Laplace equation, yields the following condition valid near the axis (terms of order \tilde{r}^2 and higher are neglected):

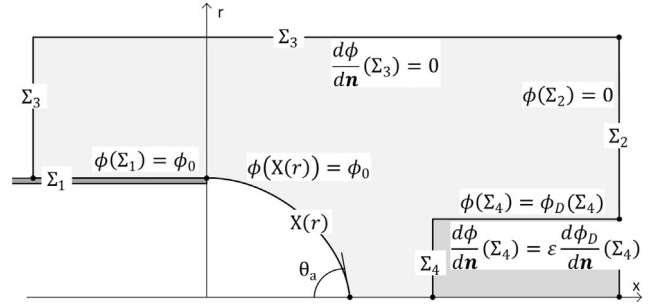


Fig. 3. Computational domain and boundary conditions.

$$\frac{\cos \theta_a}{\tilde{r}} - 2 \sin^3 \theta_a \tilde{X}_0'' - \tilde{P} = \Pi_T \tilde{E}_S(\tilde{r})^2 \quad (9)$$

In a pointed surface, $\theta_a < 90^\circ$, the dominant capillary pressure term $\cos \theta_a/\tilde{r}$ is singular at the axis and must be balanced by the electric stress. Thus the electric field near the axis must follow the power law:

$$\tilde{E}_S(\tilde{r} \rightarrow 0) = \frac{E_r}{\sqrt{\tilde{r}}} \quad (10)$$

where the parameter E_r is to be obtained from the solution. After inserting this expression in (9) and balancing separately the dominant terms, and the terms of order one, we obtain the two closure equations for the Taylor number and the dimensionless pressure:

$$\Pi_T = \frac{\cos \theta_a}{E_r^2} \quad (11)$$

$$\tilde{P} = -2 \sin^3 \theta_a \tilde{X}_0'' \quad (12)$$

Finally we impose a tip angle as the third closure relation defining jet initiation, i.e. to obtain the critical voltage. To that effect we consider two significant values: the limit $\theta_a \rightarrow 90^\circ$ associated with the initial stage of the fast transition from spherical to conical meniscus (we use $\theta_{a,S} = 89.95^\circ$ to compute a numerical solution); and the angle of a Taylor cone, $\theta_{a,T} = 49.29^\circ$. Although $\theta_{a,T}$ is the solution for a highly idealized configuration (a semi infinite, equipotential cone in which surface tension fully balances the electric stress, i.e. with zero pressure jump across the surface), experimental electrosprays exhibit angles near $\theta_{a,T}$ [25].

Pantano et al. [24] originally formulated the basic model, Eqns. (1)–(7) and (10), for solving the exact geometry of a non-emitting electrospray meniscus forming a 49.29° local angle with the axis. They brilliantly used the analytical form for the electric field at the axis (Eq. (10) above), to deal numerically with this singularity. They computed the emitter potential for $\theta_a = 49.29^\circ$ as a function of the dimensionless pressure (more exactly in terms of the dimensionless volume of the meniscus, which has a one-to-one correspondence with the pressure), and the ratio between the diameter of the emitter and the gap between the emitter and the collector. Gañán-Calvo et al. provide a functional fitting of this law in a recent review [2]. Pantano et al. do not discuss the possibility of alternative tip angles, nor of a closure condition like Eq. (12) to fix the pressure and determine the critical voltage. In fact this condition does not exist in their model because the shape of their meniscus near the axis only has the linear term in Eq. (8).

We next summarize other elements of the model and the numerical method. First, we are interested in understanding the effect of a nearby dielectric rod in the initiation of the jet. The model incorporates this by solving an additional Laplace's equation for the potential inside the rod, $\nabla^2\phi_D = 0$, while enforcing the usual jump conditions across the uncharged surface of a dielectric:

$\phi(\Sigma_4) = \phi_D(\Sigma_4)$ and $\frac{d\phi}{dn}(\Sigma_4) = \varepsilon \frac{d\phi_D}{dn}(\Sigma_4)$, where ε is the dielectric constant of the rod. Second, we solve the Laplace equation using the Boundary Element Method, BEM [26]. Since only the electric field at the free surface is needed to solve (1), the BEM technique, based on solving algebraic equations for the values of ϕ and/or $\frac{d\phi}{dn}$ at nodes on the surfaces of the domain, is more efficient than methods discretizing the Laplace equation on a grid of higher dimensionality. We discretize the surfaces using constant elements except for the one ending at the vertex of the meniscus, where the electric field is singular. In this element the electric field varies according to (10), and the BEM method provides an equation for E_r . Due to the non-linear nature of the Young-Laplace equation, the system of Eqns. (1)–(7), (11) and (12) is solved iteratively: we set the value of the angle θ_a and an initial guess for the position of the free surface; the electric field is computed next, yielding E_r as part of the solution; the Taylor number Π_T and the dimensionless pressure \tilde{P} are obtained using Eqns. (11) and (12); and the integral of the square of the residue of (1) with the updated values of Π_T , \tilde{P} , and $\tilde{E}_S(\tilde{r})$ is computed next. If the error is smaller than a desired tolerance the solution is accepted, otherwise a new position of the free surface is computed using the least-squares weighted residual method on the Young-Laplace equation, i.e. we find the position of the surface that minimizes the integral.

$$\int_0^1 \left\{ \frac{\tilde{r}\tilde{X}'' + \tilde{X}' + \tilde{X}^3}{(1 + \tilde{X}^2)^{3/2}} + [\tilde{P} + \Pi_T \tilde{E}_S(\tilde{r})]^2 \right\}^2 dr \quad (13)$$

where $\tilde{P} + \Pi_T \tilde{E}_S(\tilde{r})^2$ is evaluated with the previous solution. The new free surface is used to compute the electric field and subsequent steps, in an iterative algorithm that ends when the solution converges. The solution of the model provides the position of the free

surface $\tilde{X}(\tilde{r})$, the Taylor number Π_T , and the dimensionless pressure \tilde{P} at jet initiation for a given electrode geometry and tip angle. The critical voltage triggering the initiation of the jet is then obtained from the Taylor number.

The surface tension is needed to obtain the onset voltage from the Taylor number. The surface tension for this custom-made polymeric solution is determined from a measurement of the shape of the meniscus as a function of the pressure head in the absence of an electric field. In this case most of the meniscus surface approximates well a sphere of radius R_c , and the surface tension is balanced by the pressure head $\frac{2}{R_c}\gamma = \rho g \Delta h$, where g is the gravity acceleration and the density ρ is calculated with a mass-volume correlation, $\rho = 0.983$ g/ml. The surface tension of the polymeric solution obtained by a linear regression of the measured $\{1/R_c, \Delta h\}$ points is 0.046 N/m (see Fig. 4 in Supporting Material).

4. Results and discussion

4.1. Jet initiation modes

Fig. 4 shows photographs of the meniscus during the fast transition from spherical to conical shape preceding the ejection of the jet, taken with a high speed camera. Rows (a) and (b) are for the emitter/plate configuration, and (c) and (d) are for the emitter/rod/plate case. In rows (a), (b) and (c) the meniscus evolves towards the conical shape within milliseconds, and makes contact with the collector before releasing the jet. Upon contact the meniscus discharges reducing the electric stresses on the surface, and falls back while leaving behind a liquid bridge attached to the collector. Conversely the meniscus in row (d) becomes fully conical and releases a jet without contacting the collector, before discharging and receding back. Two features are relevant to NFES: although

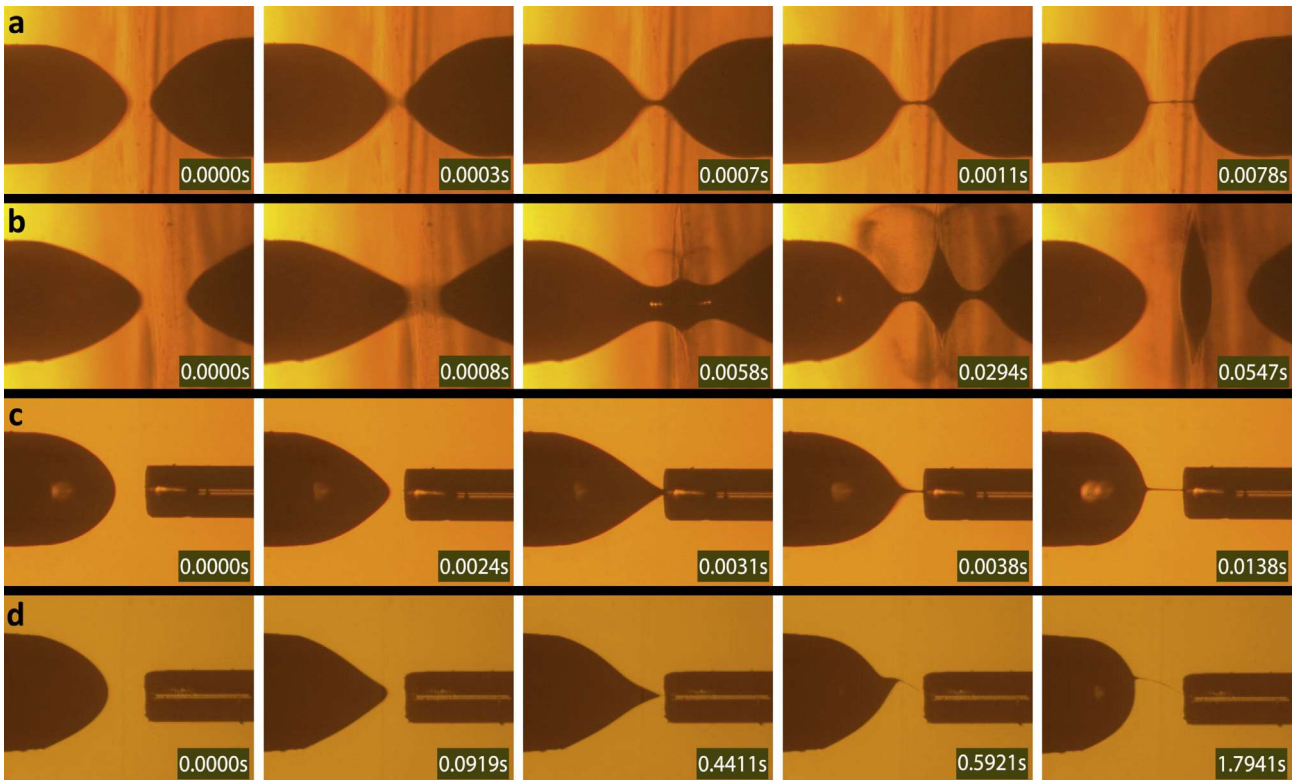


Fig. 4. High speed photographs of the liquid meniscus transitioning to a conical shape and jet formation. (a) and (b) are for the emitter/plate configuration, and emitter potentials of 500 V and 1000 V respectively. (c) and (d) are for the emitter/rod/plate configuration and emitter potentials of 1100 V and 1500 V respectively.

(a), (c) and (d) result on liquid bridges that remain attached to the collector and can be used for patterning, there are clear differences between the diameters of the jets. When the meniscus touches the collector the initial diameter of the jet must be comparable to the contact area, and the jet thins down from this initial diameter as the meniscus recedes. On the other hand the diameter of the free-forming jet in (d) is minuscule by comparison. In this case the diameter is likely associated with that for the minimum flow rate that an electrospray operating in the con-jet mode can sustain, $d_{min} \approx \left(\frac{\gamma v_0^2}{\rho k^2}\right)^{1/3} \left(\frac{\gamma^2 \rho_{sp}}{\mu^2 K}\right)^{-1/6}$ [27], a natural property that makes it possible to produce jets and fibers with diameters down to a few nanometers; K and μ stand for the electrical conductivity and the viscosity of the fluid. Secondly, although the conditions in row (b) initially produce a liquid bridge, it eventually collapses leaving behind a pool of fluid on the collector.

The evolution from a spherical to a conical meniscus and the subsequent ejection of a jet is similar for both configurations. Furthermore if the collector is sufficiently close, the tip of the meniscus contacts the collector before releasing the jet, creating also a liquid bridge as the meniscus recedes. We term *non-contact jet* and *contact jet* these two different ways of creating a liquid bridge in our experiments. Fig. 5 shows for the emitter/rod/plate configuration the instant just before the jet is initiated in both *contact jet*

and *non-contact jet* modes, at increasing value of the emitter voltage. Each photograph is for an experiment in which the emitter voltage is kept fixed, and the collector is slowly moved towards the emitter until the jet ejects. For a dielectric rod 2.23 mm long the *contact jet* mode occurs at or below a voltage of 1100 V, and the *non-contact jet* mode at 1200 V and higher potentials. The formation of the liquid bridge is more uniform and controllable in the *contact jet* mode. In this case, after the initiation happens, the conical meniscus recedes back to a spherical shape, while in the *non-contact jet* mode the shape after discharging sometimes remains non-symmetrical, probably due to the larger deformation the meniscus undergoes, preferential evaporation in the solution mixture, and its viscoelastic properties.

4.2. Effect of the shape of the electric field on the jet initiation

The collapse of the meniscus and the resulting inability to produce a liquid bridge is a phenomenon that happens frequently in the emitter/plate configuration, and seldom occurs in the emitter/rod/plate case (see Fig. 5 in Supporting Material). The behavior of the emitter/plate configuration is consistent with the perceived difficulties when using the standard jet initiation method in NFES. The different ability of the configurations for producing liquid bridges is rationalized by Fig. 6. The model is solved to find the

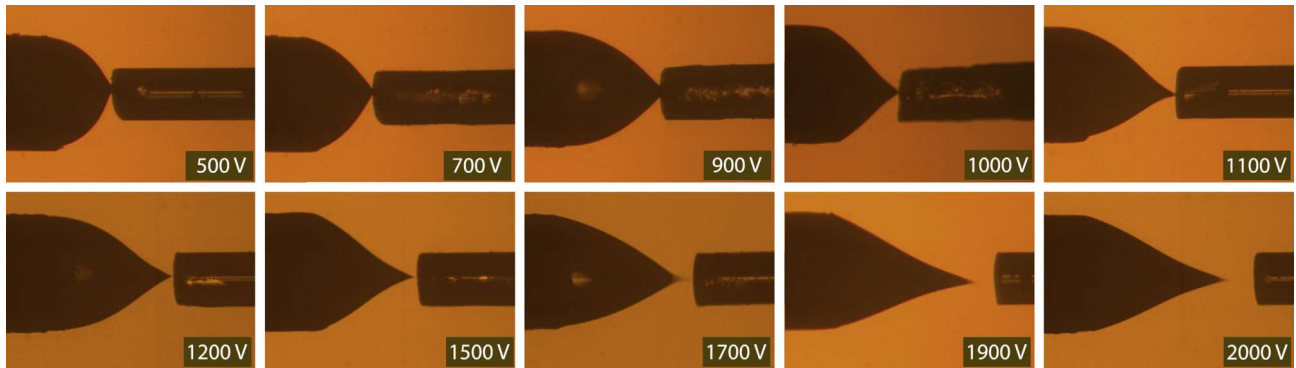


Fig. 5. Instant just before the jet is formed in the emitter/rod/plate configuration. In each case the collector is moved towards the emitter at fixed voltage. From 500 V to 1100 V the meniscus touches the rod before releasing a jet (*contact jet* mode). From 1200 V to 2000 V the jet is released from a free-standing conical meniscus (*non-contact jet* mode).

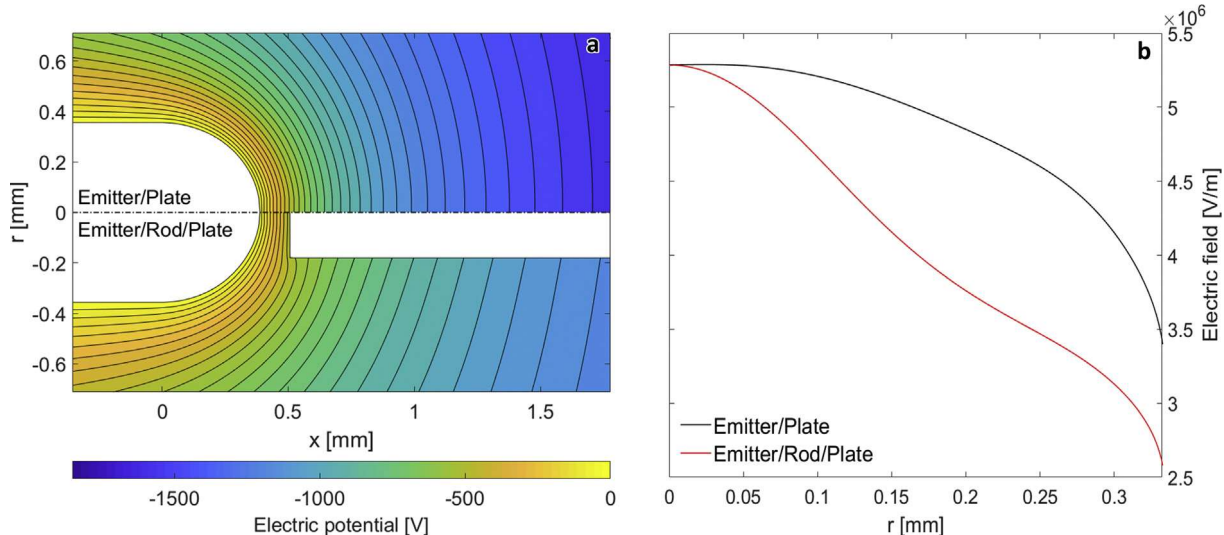


Fig. 6. (a) Electric potential surrounding the meniscus for the emitter/plate (top half) and emitter/rod/plate (bottom half) configurations at jet initiation, for a tip angle of 89.95°. The gaps between emitter and grounded plate are identical (2.73 mm). Contour lines are 50 V apart; (b) electric field on the free surface for both configurations.

potential field at jet initiation for both configurations, using $\theta_{a,S} = 89.95^\circ$ for the tip angle and a gap between emitter and plate of 2.73 mm; the length of the rod is 2.23 mm. Fig. 6(a) plots the solutions for the emitter/plate and emitter/rod/plate configurations above and below the axis of symmetry respectively. The model yields onset voltages of 1893 V for the emitter/plate configuration, and 1407 V for the emitter/rod/plate case. The dielectric rod changes the potential contours, making the field around the meniscus less spherical. Furthermore the rod induces an electric field near the axis identical to that of the emitter/plate configuration, at a significant lower voltage difference between the emitter and the grounded plate (1407 V vs 1893 V). The positions of the free surfaces for each configuration correspond to the numerical solutions, but they are indistinguishable at the length scale of the figure. Fig. 6(b) shows the electric field on the surface: both configurations have a common value of 5.34×10^6 V/m near the axis, before diverging as $r^{-1/2}$ (the plots do not show the divergence due to the smallness of the region where this occurs). At larger values of r the two electric fields separate, with the one for the emitter/plate configuration being significantly larger and nearly spherical along a significant fraction of the meniscus. Thus, while the deformation of the meniscus required to balance the electric stress is localized near the axis in the emitter/rod/plate configuration, the deformation for the emitter/plate case is more intense everywhere else. The larger deformation is more likely to lead to the collapse of the meniscus as the electric pulling is intensified to reach the jet emission condition. Note also that the stress scales as the square of the electric field, and therefore the differences in Fig. 6(b) are magnified in the stress. The convergence of the electric fields near the axis for both configurations is an interesting feature of Fig. 6(b). Since the inclusion of the dielectric rod makes the geometry quite different and introduces a dependency on the dielectric constant, the convergence near the axis suggests that the electric field at the tip at jet initiation is determined by local properties alone. In fact, the dominant balance in (9) requires a dimensional field near the axis $E_S(r \rightarrow 0) = \left(\frac{2\gamma \cos \theta_a}{\epsilon_0 r}\right)^{1/2}$, i.e. a field solely determined by the tip angle and the surface tension, and which does not depend on other factors such as the radius of the emitter, the gap between emitter and collector, or the dielectric constant of the rod. The common shape of the field near the axis separates at increasing distance from the axis, responding to the values of the emitter-collector gap and the presence of the dielectric rod.

4.3. Critical voltage law

Fig. 7 compares the relation between the critical voltage and the gap separating meniscus and collector, found in experiments and with the model, for the emitter/plate and the emitter/rod/plate configurations. Although the gap between emitter and collector is a more direct choice to define the critical voltage law, the experimental critical voltage is less repeatable when using this distance. This is due to the viscoelastic nature of the solution, which makes it difficult to control the size and shape of the meniscus at zero electric field, and introduces a large uncertainty when establishing the position of an effective emitter rim. The emitter/rod/plate configuration considers both closure equations for the tip angle, $\theta_{a,S} = 89.95^\circ$ and $\theta_{a,T} = 49.29^\circ$. The emitter/plate configuration does not consider $\theta_{a,T} = 49.29^\circ$ because it only operates reliably in contact jet mode, i.e. if the meniscus fully evolves into a cone before touching the collector the probability for creating a lasting liquid bridge is small. The experimental initiation distance for $\theta_{a,S} = 89.95^\circ$ is defined as the gap between the spherical meniscus and the collector just before the meniscus abruptly turns conical,

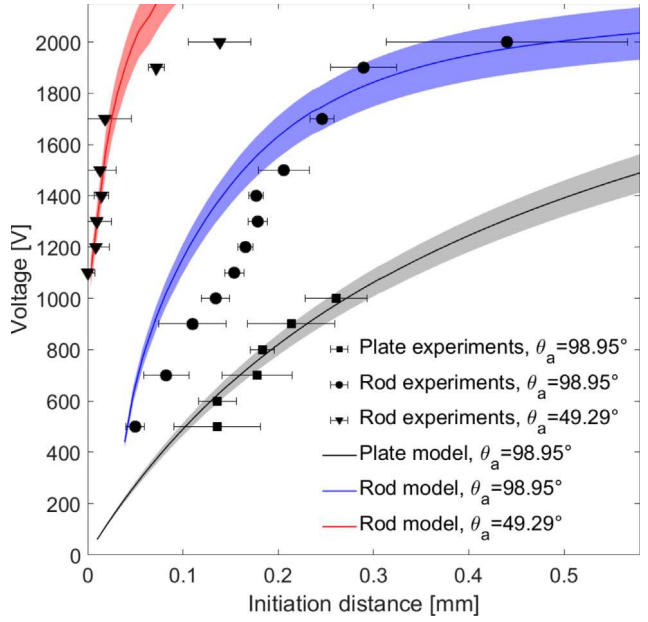


Fig. 7. Comparison of the experimental and model critical voltage laws (emitter potential vs gap between meniscus and collector at jet initiation) for the emitter/plate and emitter/rod/plate configurations. The envelopes of the shaded areas correspond to a surface tension $\pm 10\%$ of the nominal value.

while for $\theta_{a,T} = 49.29^\circ$ we use the shortest gap recorded with the high speed camera once the meniscus turns conical. The agreement between experiments and model results is good for the emitter/plate configuration when using $\theta_{a,S} = 89.95^\circ$ as the criterion for jet initiation. The agreement for the emitter/rod/plate configuration is also good for both tip angles, although $\theta_{a,S} = 89.95^\circ$ yields a better agreement at the largest initiation distances. The model also captures well the onset voltage at which the tip of the cone just touches the rod, $V_{ON} = 1040$ V from the model and between 1100 V and 1200 V in experiments, as shown by the $\theta_{a,T} = 49.29^\circ$ solution. When using $\theta_{a,T} = 49.29^\circ$ the model cannot compute onset voltages lower than 1040 V because the meniscus crosses the surface of the rod.

5. Conclusion

The jets typical of NFES and cone-jet electrosprays develop once a critical emitter potential triggers a sudden transformation of the spherical meniscus into a cone. The jet is emitted from the vertex of the meniscus. The first principles model described in this article reproduces the conditions leading to the initiation of the jet. In particular, it is able to calculate for the first time the critical voltage for a given electrode geometry and surface tension. Existing models yield an undetermined system of equations (e.g. in Ref. [28] the height of the meniscus must be obtained from experiments, while Ref. [24] computes emitter potentials for given values of the volume of the meniscus), or consider a semi-infinite geometry from which the critical voltage of an experimental configuration cannot be recovered [25,29]. The model solves the coupled Young-Laplace equation for the free surface and the Laplace equation for the electric potential surrounding it, and is adaptable to any axisymmetric configuration. Thus it can be used to optimize the initiation of the jet and the subsequent deposition of fibers, as demonstrated by the analysis and experiments of the emitter/plate and emitter/rod/plate configurations: the numerical solution shows how the insertion of a dielectric rod focuses the electric field near the axis, reducing the area of the meniscus affected by strong electric fields,

stresses and deformations, and preventing the collapse of the meniscus. We have studied two different ways of creating a liquid bridge between meniscus and collector: in *non-contact jet* mode the jet is ejected from a fully conical meniscus, moves forward and attaches to the collector; while in the novel *contact jet* mode the tip of the meniscus touches the collector before it can become fully conical, leaving attached a liquid bridge as it recedes upon discharging. *Non-contact jet* mode produces the thinnest jets, with initial diameters that likely depend on the properties of the fluid alone according to the law $d \approx \left(\frac{\gamma_0^2}{\rho K}\right)^{1/3} \left(\frac{v^2 \rho g_0}{\mu K}\right)^{-1/6}$ [27]. *Contact jet* mode produces a bridge with an initial diameter of the order of the meniscus/collector contact region, and can be used as an alternative to mechanically-aided initiation techniques requiring the insertion of a sharp tip in the meniscus [17,22,23]. The model and the experimental observations described in this work will support the development of near-field electrospinning on the basis of first principles. A particularly interesting problem is demonstrating that the jet diameter law for cone-jets is applicable to the polymeric solutions typical in electrospinning, so that the properties of the fluid can be designed to produce jets and fibers of the desired diameters down to a few nanometers, when operating in *non-contact jet* mode. The optimization of the electrostatic field made possible by the model will help solving this problem.

Acknowledgements

The funding source is NSF's Fluid Dynamics Program (USA), grant CBET-1604163.

Appendix A. Supplementary material

Supplementary data to this article can be found online at <https://doi.org/10.1016/j.jcis.2019.02.041>.

References

- [1] D.H. Reneker, I. Chun, Nanometre diameter fibres of polymer, produced by electrospinning, *Nanotechnology* 7 (1996) 216–223.
- [2] A.M. Gañán-Calvo, J.M. López-Herrera, M.A. Herrada, A. Ramos, J.M. Montanero, Review on the physics of electrospray: from electrokinetics to the operating conditions of single and coaxial Taylor cone-jets, and AC electrospray, *J. Aerosol Sci.* 125 (2018) 32–56.
- [3] M. Magnani, M. Gamero-Castaño, Numerical simulation of electrospraying in the cone-jet mode, *J. Fluid Mech.* 859 (2019) 247–267.
- [4] T.J. Sill, H.A. von Recum, Electrospinning: applications in drug delivery and tissue engineering, *Biomaterials* 29 (2008) 1989–2006.
- [5] Q.P. Pham, U. Sharma, A.G. Mikos, Electrospinning of polymeric nanofibers for tissue engineering applications: a review, *Tissue Eng.* 12 (2006) 1197–1211.
- [6] D. Li, Y. Xia, Direct fabrication of composite and ceramic hollow nanofibers by electrospinning, *Nano Lett.* 4 (2004) 933–938.
- [7] R. Gopal, S. Kaur, Z. Ma, C. Chan, S. Ramakrishna, T. Matsuura, Electrospun nanofibrous filtration membrane, *J. Membr. Sci.* 281 (2006) 581–586.
- [8] X.H. Qin, S.Y. Wang, Filtration properties of electrospinning nanofibers, *J. Appl. Polym. Sci.* 102 (2006) 1285–1290.
- [9] B. Ding, M. Wang, J. Yu, G. Sun, Gas sensors based on electrospun nanofibers, *Sensors* 9 (2009) 1609–1624.
- [10] B. Ding, J. Kim, Y. Miyazaki, S. Shiratori, Electrospun nanofibrous membranes coated quartz crystal microbalance as gas sensor for NH₃ detection, *Sensor. Actuat. B-Chem.* 101 (2004) 373–380.
- [11] B. Ding, M. Wang, X. Wang, J. Yu, G. Sun, Electrospun nanomaterials for ultrasensitive sensors, *Mater. Today* 13 (2010) 16–27.
- [12] E. Formo, E. Lee, D. Campbell, Y. Xia, Functionalization of electrospun TiO₂ nanofibers with Pt nanoparticles and nanowires for catalytic applications, *Nano Lett.* 8 (2008) 668–672.
- [13] D. Sun, C. Chang, S. Li, L. Lin, Near-field electrospinning, *Nano Lett.* 6 (2006) 839–842.
- [14] X. He, J. Zheng, G. Yu, M. You, M. Yu, X. Ning, Y. Long, Near-field electrospinning: progress and applications, *J. Phys. Chem. C* 121 (2017) 8663–8678.
- [15] A.L. Yarin, S. Koombhongse, D.H. Reneker, Bending instability in electrospinning of nanofibers, *J. Appl. Phys.* 89 (2001) 3018–3026.
- [16] X. Wang, G. Zheng, G. He, J. Wei, H. Liu, Y. Lin, J. Zheng, D. Sun, Electrohydrodynamic direct-writing ZnO nanofibers for device applications, *Mater. Lett.* 109 (2013) 58–61.
- [17] G.S. Bisht, G. Canton, A. Mirsepasi, L. Kulinsky, S. Oh, D. Dunn-Rankin, M. Madou, Controlled continuous patterning of polymeric nanofibers on three-dimensional substrates using low-voltage near-field electrospinning, *Nano Lett.* 11 (2011) 1831–1837.
- [18] L. Ferrer-Argemi, E. Aliabadi, A. Cisquella-Serra, A. Salazar, M. Madou, J. Lee, Size-dependent electrical and thermal conductivities of electro-mechanically-spun glassy carbon wires, *Carbon* 130 (2018) 87–93.
- [19] C. Hellmann, J. Belardi, R. Dersch, A. Greiner, J.H. Wendorff, S. Bahnmueller, High precision deposition electrospinning of nanofibers and nanofiber nonwovens, *Polymer* 50 (2009) 1197–1205.
- [20] Y. Xin, D.H. Reneker, Hierarchical polystyrene patterns produced by electrospinning, *Polymer* 53 (2012) 4254–4261.
- [21] T.P. Lei, X.Z. Lu, F. Yang, Fabrication of various micro /nano structures by modified near-field electrospinning, *AIP Adv.* 5 (2015) 041301.
- [22] C. Chang, K. Limkraillassiri, L. Lin, Continuous near-field electrospinning for large area deposition of orderly nanofiber patterns, *Appl. Phys. Lett.* 93 (2008) 1–4.
- [23] G. Zheng, W. Li, X. Wang, D. Wu, D. Sun, L. Lin, Precision deposition of a nanofibre by near-field electrospinning, *J. Phys. D: Appl. Phys.* 43 (2010) 415501.
- [24] C. Pantano, A.M. Gañán-Calvo, A. Barrero, Zeroth-order, electrohydrostatic solution for electrospraying in cone-jet mode, *J. Aerosol Sci.* 25 (1994) 1065–1077.
- [25] J. Fernández de la Mora, The effect of charge emission from electrified liquid cones, *J. Fluid Mech.* 243 (1992) 561–574.
- [26] A.A. Bakr, *The Boundary Integral Equation Method in Axisymmetric Stress Analysis Problems*, Springer, Chap. II, 1986.
- [27] A.M. Gañán-Calvo, N. Rebollo-Muñoz, J.M. Montanero, The minimum or natural rate of flow and droplet size ejected by Taylor cone-jets: physical symmetries and scaling laws, *New J. Phys.* 15 (2013) 033035.
- [28] A.L. Yarin, S. Koombhongse, D.H. Reneker, Taylor cone and jetting from liquid droplets in electrospinning of nanofibers Taylor cone and jetting from liquid droplets in electrospinning of nanofibers, *J. Appl. Phys.* 90 (2001) 4836–4846.
- [29] G.I. Taylor, Disintegration of water drops in an electric field, *Proc. R. Soc. Lond. A* 280 (1964) 383–397.